Gradient-Index-Based Frequency-Coded Retroreflective Lenses for mm-Wave Indoor Localization

PETR KADERA[1,*], (Graduate Student Member, IEEE),
ALEJANDRO JIMÉNEZ-SÁEZ[2,*], (Graduate Student Member, IEEE), **TOM BURMEISTER**[2],
JAROSLAV LACIK[1], (Member, IEEE), **MARTIN SCHÜßLER**[2], (Member, IEEE),
AND ROLF JAKOBY[2], (Member, IEEE)

[1]Department of Radio Electronics, Brno University of Technology, 612 00 Brno, Czech Republic
[2]Institute of Microwave Engineering and Photonics, Technische Universität Darmstadt, 64283 Darmstadt, Germany

Corresponding authors: Petr Kadera (kadera@feec.vutbr.cz) and Alejandro Jiménez-Sáez (alejandro.jimenez_saez@tu-darmstadt.de)

*Petr Kadera and Alejandro Jiménez-Sáez contributed equally to this work.

ABSTRACT This article introduces retroreflective lenses for millimeter-wave radio-frequency indoor localization. A three-dimensional (3D) gradient-index Luneburg lens is employed to increase radar cross section (RCS) of photonic-crystal high-Q resonators and its performance is compared to conventional radar retroreflectors. A classic Luneburg lens with and without a reflective layer is realized with 25 mm diameter ($6.7\,\lambda_0$), showing a realized gain of 24.6 dBi and a maximum RCS of -9.22 dBm^2 at 80 GHz. The proposed Luneburg lens with embedded high-Q resonators as frequency-coded particles in a photonic crystal structure, operating as a reflective layer, achieved a maximum RCS of -15.84 dBm^2 at the resonant frequency of 76.5 GHz and showed a repeatable response each 18° over ±36° in two perpendicular planes. With this high RCS of the Luneburg lens, a maximum readout range of 1.3 m could be achieved compared to 0.15 m without the lens at 76.5 GHz for the same transmit power, receiver sensitivity, and gain of the reader antenna.

INDEX TERMS Gradient-index, luneburg lens, retroreflective lens, retroreflector, photonic crystal, chipless RFID, indoor localization, mmWave, RCS enhancement, artificial dielectric.

I. INTRODUCTION

Retroreflectors are devices providing radar cross section (RCS) augmentation and are widely used for automotive radars and measurement calibration [1], tracing objects [2], indoor localization [3] and recently, they have been explored as devices which can help to overcome high path losses at 5G millimeter waves and optical communication systems [4].

For applications such as indoor localization using passive retroreflectors, a self-localizing device (in the following reader) interrogates each retroreflector and determines its relative distance to it. With the relative distance to several retroreflectors and a database of the positions of the retroreflectors in the room or building, the reader can precisely calculate its position [3].

The associate editor coordinating the review of this manuscript and approving it for publication was Davide Comite.

Such retroreflectors can become smaller with the wavelength, while the accuracy of radar ranging algorithms increases at higher frequencies due to the higher absolute bandwidth [5]. For these reasons, the realization of retroreflectors in the mm-wave (30 GHz to 300 GHz) frequency range has received increasing attention [6], [8]–[12].

For successful localization, the reader must identify each retroreflector to find their position in the database. This target identification in radar has been intensively investigated for decades with either active or passive methods. In an indoor self-localization environment, passive methods are advantageous due to the absence of a battery, i.e., no maintenance needed. A simple solution is the realization of mm-wave retroreflectors to generate one or several notches in an otherwise frequency-stable backscattering response of trihedral corner reflectors [6], [8], [10].

Despite their high RCS, the identification of passive retroreflectors can be unstable due to strong reflections in the

nearby environment, i.e., clutter, such as naturally occurring retrodirective reflections in the corners of a room or among furniture. To overcome this issue, high quality factor (high-Q) resonators can be exploited for their ability to store electromagnetic (EM) energy for a longer time inside the resonator, which helps to filter out the undesired clutter reflections by a time-gating technique as presented in [13]–[15]. The realization of high-Q resonators at mm-wave frequencies for identification by photonic-crystal (PhC) structures is presented in [16]. However, the small geometrical size of the resonators results in a reduction of their RCS, limiting the range achieved by single-resonator tag landmarks at 90 GHz to less than 20 cm.

In order to increase RCS, arrays of high-Q resonators can be integrated with corner reflectors as in [11]. However, for high-Q resonators, even small variations in the resonance frequency of some resonators or temperature gradients result in a large variation in the phase of the re-radiated signal by each resonator, which strongly reduces RCS. This effect worsens the higher Q-factor due to the inherently narrowband response $Q = f_{resonance}/\Delta f$. For this reason, the combination of high-Q dielectric resonators with low loss dielectric lenses is desired. By placing the high-Q resonator coding tags near the focal area of the lens, only one or a few coding parts are excited at a certain moment, so that manufacturing tolerances do not affect RCS and only have an effect on the coding density given by bits per GHz. The larger the manufacturing tolerances are, the more bandwidth needs to be used for a single resonance frequency, i.e. a bit.

A simple homogeneous fused silica ball lens presents a focal area near its opposite end and can be used as a retroreflector. However, its constant relative permittivity ($\epsilon_r \approx 4$) limits its use to small diameters of 4-5 wavelengths due to a high-density of parasitic resonances, which are caused by an impedance mismatch at its surface [17]. To overcome this limiting factor, a Luneburg lens with a gradient permittivity profile can be used as theoretically introduced in [18]. A schematic model representing this system with two frequency coded tag landmarks is shown in Fig. 1. Our previous work in [19] considered for RCS enhancements a 2D Luneburg lens, which has operation limited only at azimuthal plane, with small spherical low-Q dielectric resonators at a lower frequency band around 5.5 GHz, providing low coding density and short ringing time to differentiate its RCS response in the time-domain.

In this article, the design and manufacturing of a 3D Luneburg lens and its integration with 5 high-Q PhC coding tags at 80 GHz for frequency coding is presented. Depending on the angle of arrival of the interrogation signal, one of the coding tags is excited, demonstrating the potential of this approach for passive frequency-coded retroreflectors with larger ranges, higher and stable angular coverage in selected planes of the second half of the lens, and allowing for an effective clutter suppression.

This article is organized as follows: Section II presents a comparison of various retroreflectors used for the realization
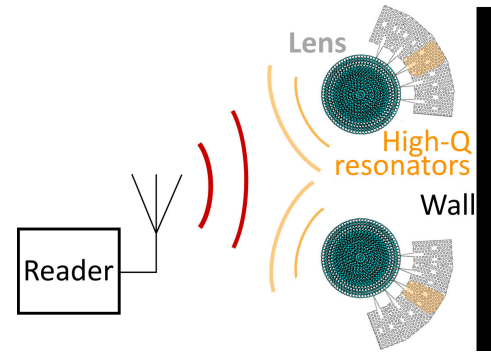

FIGURE 1. Interrogation system with two of the proposed high-RCS retroreflective lenses with embedded high-Q resonators as frequency-coded particles in a PhC structure, operating as a reflective layer.

of high-RCS frequency-coded retroreflectors, and their performance is discussed in terms of RCS pattern. In addition, the design of the Luneburg lens is introduced, and its performance is characterized first as an antenna and then as a retroreflector with an additional reflective layer. Section III focuses on the combination of PhC high-Q resonators for the realization of frequency-coded Luneburg lens reflectors. The proposed designs are manufactured, and the measurement results are shown in Section IV, following a discussion of the results and their intended improvement with a three-dimensional (3-D) printing technology.

II. RETROREFLECTORS

In the field of radar systems, there are mainly three types of retroreflectors. The first type is a corner reflector, which is mainly used for radar calibrations and can be constructed in dihedral, trihedral triangular or trihedral cubical forms [20]. They provide large RCS in a limited angular range of up to about ±45°. The second type is a spherical reflector which is usually made as a metallic sphere or dielectric lens with a constant or gradient refractive index [21]. They provide a very wide angular range, but their RCS is usually lower. The third type of retroreflectors is the Van Atta array which can be very thin with comparable RCS as the Luneburg lens, but it requires a complex connection network between particular array segments and its fabrication at mm-wave frequencies is difficult [22]. The RCS patterns of the selected retroreflectors at a frequency of 80 GHz will be presented in this chapter.

A. METALLIC RETROREFLECTORS

The monostatic RCS of conventional metallic reflectors as trihedral triangular and cubical corner reflector, flat reflector and metallic sphere reflector, at the boresight as in Fig. 2, can be calculated by the expressions (1)-(4), respectively [20], [23]:

$$\sigma_{\text{tiangular}} = 10 \log\left(\frac{4\pi}{\lambda^2} \cdot \frac{a^4}{12}\right) \quad [\text{dBm}^2], \quad (1)$$
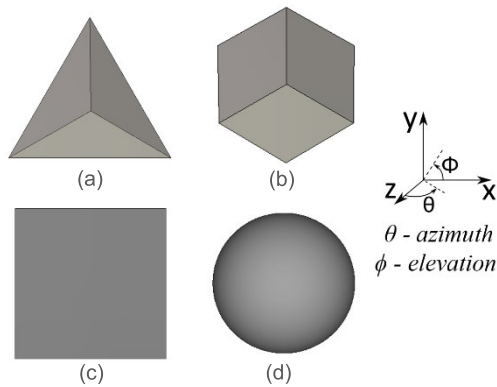
FIGURE 2. Trihedral triangular corner reflector (a), trihedral cubical corner reflector (b), flat reflector (c), sphere reflector (d).

TABLE 1. Monostatic RCS comparison of selected retroreflectors at a frequency of 80 GHz. Edge length / diameter = 25 mm.

Reflector type	Maximum RCS [dBm^2] (analyt.)	Maximum RCS [dBm^2] (num.)	Azimuthal angular range [°] (num.)
Triangular corner	-15.36	-15.5	±26.5
Cubical corner	0.2	0.12	±18
Flat	-1.23	-1.41	±2.15
Sphere	-33.09	-32.9	±180

[8], or microstrip coding [9], but this type of reflectors share the abrupt RCS decay for directions other than broadside of the flat metal reflector. However, the strong variation of RCS with the angle and the inability to distinguish the corner reflector's response from nearby clutter are restrictive. These issues are addressed with the Luneburg lens design presented in the next section.

B. RETROREFLECTIVE LUNEBURG LENS

The Luneburg lens has a spherical shape with a gradient permittivity profile, which allows to focus an incident plane wave in a so-called focal area on the opposite end of the lens. When this opposite side of the lens is covered by a reflective layer, the focused power is reflected back in the direction of incidence. In this case, it operates as a retroreflective lens. An advantage compared to corner retroreflectors is its more stable RCS for varying azimuthal and elevation angles. Compared to homogeneous spherical dielectric lenses, the gradient-index profile avoids impedance mismatch [24], i.e., structural reflections of the incoming wave, so that its maximum size is not restricted by the number of wavelengths as in [17]. In comparison with an omnidirectional retroreflective Eaton lens, the Luneburg lens requires materials with effective permittivity varying from 2 (in the middle) to 1 (at the edge), what is manufacturable by conventional methods, whereas the Eaton lens requires effective permittivity profile varying from infinity to 1, which can be transformed by transformation-optics methods to more convenient profile of effective parameters [25]. However, the main disadvantage of this process is requirement for anisotropic metamaterials which are generally narrowband and thus not feasible for broadband applications such as multi-bit mmWave frequency-coded retroreflectors. Other examples of retroreflective lenses, which are used in optics, includes a Cat's eye reflector with a relatively high acceptance angle of ±60° [26], or micromachined sheet containing spherical microlenses and micromirrors allowing acceptance angle of ±37° [28]. The Luneburg lenses can overall provide the best performance and their main limiting factor during designing is the fabrication complexity due to the presence of numerous small details.

The gradient permittivity profile of the Luneburg lens varies continuously in the radial direction, r, according to the following expression [24]:
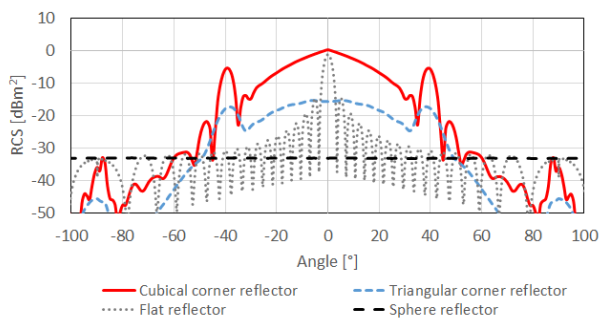

FIGURE 3. Azimuthal monostatic RCS pattern of the considered reflectors.

$$\sigma_{\text{cubical}} = 10 \log \left(\frac{12\pi a^4}{\lambda^2} \right) \quad [\text{dBm}^2], \tag{2}$$

$$\sigma_{\text{flat}} = 10 \log \left(\frac{4\pi a^4}{\lambda^2} \right) \quad [\text{dBm}^2], \tag{3}$$

$$\sigma_{\text{sphere}} = 10 \log \left(\pi R^2 \right) \quad [\text{dBm}^2], \tag{4}$$

where σ denotes *RCS* of the given retroreflector, a denotes the side length, R denotes the lens radius and λ is the wavelength.

For a comparison with the designed Luneburg lens, the edge length of the triangular and cubical corner and flat reflectors is set to 25 mm, and the diameter of the sphere reflector is 25 mm. The monostatic RCS patterns of the selected retroreflectors at a frequency of 80 GHz ($\lambda = 3.75$ mm) are shown in Fig. 3 and their performance is summarized in Tab. 1. An asymptotic solver (CST Studio Suite) with the Shooting Bouncing Ray method has been used for numerical simulations to determine angular range defined as an angle of 6 dB decay from the maximum RCS value.

From the previous comparison, it can be concluded that the highest RCS is achieved by the trihedral cubical corner reflector. Coding in corner reflectors can be achieved by frequency selective surfaces [6], dielectric resonators [11], or thin film modulators [7] with high RCS for applications such as indoor localization. Similarly, coding in flat plate reflectors can be achieved by a frequency selective surface plate, a planar dielectric resonator array in front of a metal plate

$$\varepsilon_{\text{r}}(r) = 2 - \left(\frac{r}{R} \right)^2, \tag{5}$$

where ε_r denotes the relative permittivity and R is the radius of the lens.

The monostatic RCS of the retroreflective Luneburg lens at the boresight can be calculated by equation (6).

$$\sigma_{\text{Lumeburg}} = 10 \log \left(\frac{4\pi \left(\pi R^2 \right)^2}{\lambda^2} \right), \quad [\text{dBm}^2] \qquad (6)$$

Thus, for a lens diameter of 25 mm or 6.7 λ_0, being λ_0 the wavelength in a vacuum at 80 GHz, the maximal RCS level of -6.67 dBm^2 can be achieved for the retroreflective Luneburg lens.

In practice, this relative permittivity profile in equation 4 is achieved by patterning the sub-wavelength profile, i.e., by reducing the amount of the high-permittivity material. Due to the small patterning compared to the wavelength, the optically heterogeneous structure presents homogeneous characteristics at the targeted bandwidth. In this work, the ideal Luneburg lens permittivity profile is discretized into 15 layers, which can provide sufficient profile approximation. The layers are numbered from 0 to 15, where the 0$^{\text{th}}$ layer is in the lens center and the 15$^{\text{th}}$ layer is at the lens's edge. To realize a 3D lens design, 31 perforated 2.5D layers of dielectric substrate are stacked together to copy the spherical shape of the lens. Each layer consists of a certain number of rings composed of unit-cells with subwavelength dimensions (0.9 mm $\times$ 0.9 mm) on a dielectric substrate Rogers RT5880 (thickness $t = 0.787$ mm, $\varepsilon_r = 2.24$, tan $\delta = 0.0037$), which is characterized by a transmission/reflection method in a WR-10 rectangular waveguide at a frequency of 80 GHz [28]. A stepped approximation of the desired permittivity profile is realized by holes with diameters between 0.4 mm and 0.85 mm. The minimum spacing between two adjacent unit-cells is 0.1 mm. The effective relative permittivity in the polarization direction with the E-field parallel/perpendicular to the height of the cylindrical holes is obtained from a dispersion diagram by numerical simulations [29]. This construction approach is selected on the basis of our previous experience with fabrication of gradient-index based lenses at mm-wave frequencies, which require very small building unit-cells (size of maximally about $\lambda/3$ in the given material $\approx$0.84 mm at 80 GHz), low permittivity and low loss material such as Teflon, HDPE or Rexolite. The most feasible way of construction and design is therefore as stacked perforated dielectric substrates similarly as in [30]. Another construction options are generally based on an additive manufacturing, where the building unit-cells can be of various shapes as cubes (Polymer Jetting - PJ) [31], cuboid grid (Fused Decomposition Modeling - FDM) [32] or 3D crosses (Stereolithography - SLA) [33]. However, it is hard to realize such structures at mm-waves above 80 GHz because of the *xy* resolution limit of the conventional 3D printers for reliable printing (FDM $\approx$ 0.4 mm depending on the print nozzle diameter [34], SLA $\approx$ 0.15 mm depending on the laser spot size [35]), and the requirement for supporting structures, which are too difficult to remove. Further, a higher permittivity ($\varepsilon_r > 2.5$)
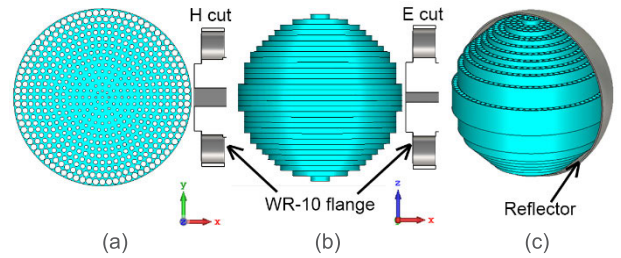

FIGURE 4. The model of a perforated Luneburg lens, cut in the middle (a), side view of the Luneburg lens (b), retroreflective Luneburg lens with reflective layer (c).
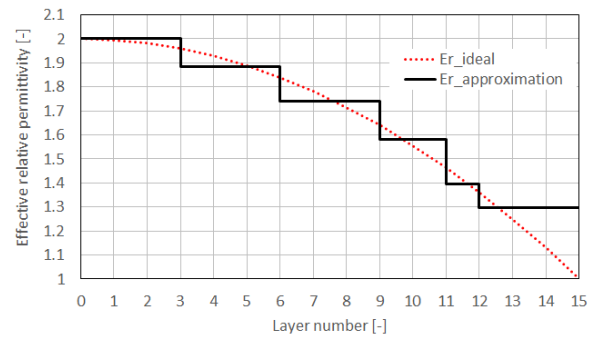

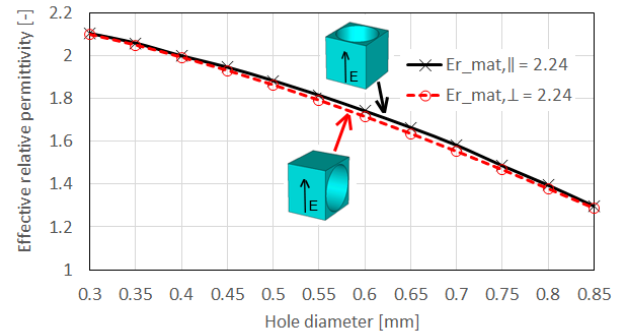**FIGURE 5.** Discretized permittivity profile of the perforated Luneburg lens.

FIGURE 6. Effective relative permittivity of the perforated dielectric substrate unit-cell with dimensions 0.9 mm $\times$ 0.9 mm $\times$ 0.787 mm.

and dielectric losses (tan $\delta > 0.02$) of the materials used in additive manufacturing makes this method inappropriate [36]–[38].

To verify the Luneburg lens performance, an antenna configuration with WR-10 waveguide excitation is assumed. The Luneburg lens as an antenna and as a reflector with its permittivity profile are depicted in Figs. 4-5. The corresponding dependence of the effective relative permittivity on hole diameter is shown in Fig. 6. The simulated far-field radiation pattern for azimuthal position (Fig. 4 a) and elevation position (lens rotated around the *x* axis by 90 degrees) is shown in Fig. 7.

The simulated monostatic RCS pattern of the retroreflective lens with a 150° aluminum cup is shown in Fig. 8. The electric field amplitudes inside the lens with and without
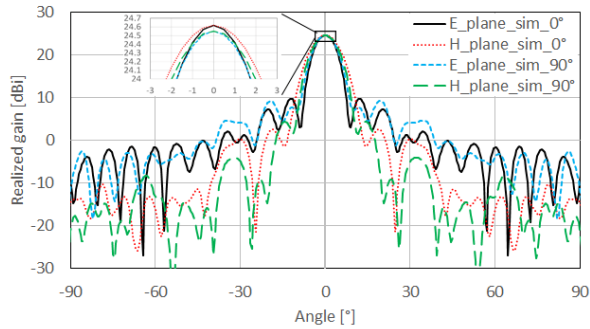
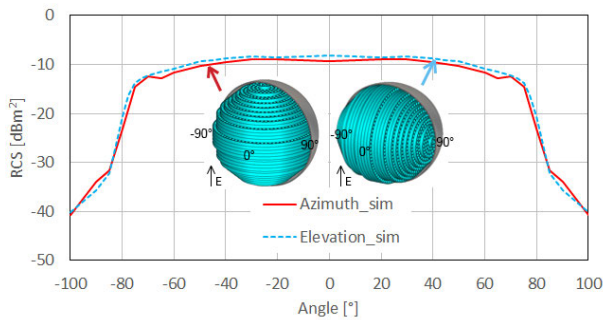**FIGURE 7.** Simulated far-field radiation pattern of the perforated Luneburg lens.

FIGURE 10. Electric field inside the perforated Luneburg lens with a reflective layer (x-y plane cut), *f* = 80 GHz.

FIGURE 8. Simulated RCS pattern of the perforated retroreflective Luneburg lens.
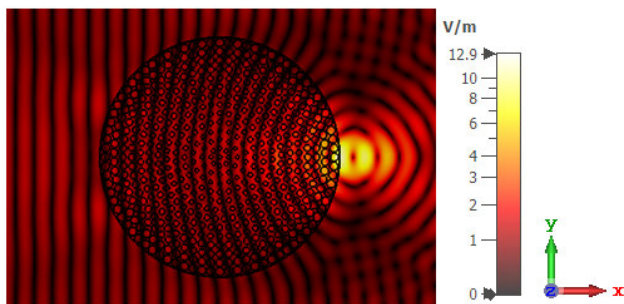

FIGURE 9. Electric field inside the perforated Luneburg lens (x-y plane cut), *f* = 80 GHz.

a reflective layer at the backside are shown in Figs. 9-10. A plane wave excitation with the wave propagation in the x direction and E vector in z direction is assumed.

The maximum simulated realized gain of the Luneburg lens placed in front of a WR-10 rectangular waveguide at 80 GHz is 24.62 dBi. The dielectric losses cause a decrease in gain of 0.58 dB and impedance mismatch loss ($S_{11} = -16$ dB) cause a decrease in gain of 0.11 dB. The metallic losses in the waveguide due to finite conductivity ($\sigma_{Ag} = 4.56 \cdot 10^7$ S/m) lead to a further decrease in gain of 0.12 dB. The simulated side lobe levels in E-plane and H-plane are -14.8 dB and -22.1 dB in azimuthal position and -15.3 dB and -20.2 dB in elevation position, respectively. A small discrepancy of realized gain for the lens orientation 0° and 90° is
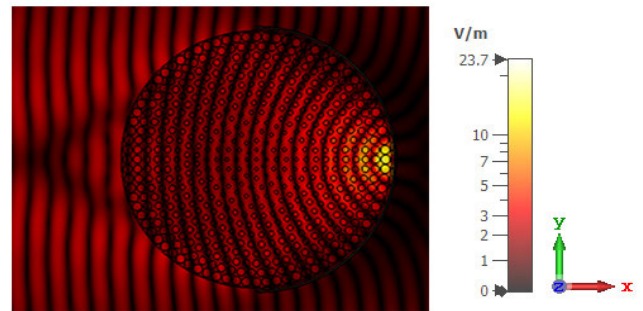
attributed to the slight dielectric anisotropy of the perforated substrate. For the retroreflective Luneburg lens, the simulated monostatic RCS level in azimuthal and elevation planes is stable in the angular range of $\pm 75°$ (-6 dB), with a maximum value of -8.14 dBm^2(assuming an aluminum covering layer with a surface roughness of 20 μm). A discrepancy between azimuth and elevation plane at 0° is ascribed to an effect of dielectric anisotropy and the fact that for the simulation of the elevation plane was the lens oriented in 90° position to correspond with the practical position during measurement (see Fig. 12 e). This angular stability is in good agreement with values found in literature [20], [24]. The intensity of the electric field is doubled after covering the lens with a reflective layer due to the full reflection of the incident EM wave. The following section will introduce the Luneburg lens with embedded frequency-coded PhC high-Q resonators as a reflective layer.

III. RETROREFLECTIVE HIGH-Q TAG LANDMARKS
PhC-based 2-bit high-Q coding tags have been designed to be integrated with the Luneburg lens. The coding tags are designed by coupling two PhC high-Q resonators to a dielectric waveguide, which is terminated by a rod antenna. By placing the rod antenna in the focal area of the Luneburg lens, the interrogation signal is fully coupled into one or a few high-Q coding tags, therefore increasing their RCS, i.e., the maximum readout range. Since the focal area of the lens depends on the orientation towards the reader, multiple high-Q coding tags are placed around the lens, increasing the angular coverage. The high-Q resonators are designed as described in [39] to resonate at slightly different resonance frequencies so that both resonances can be distinguished in the frequency spectrum. Notice that only one or a few of the coding tags are excited for a certain interrogation angle, so that potential manufacturing inaccuracies only have a local effect on the RCS response for certain interrogation angles.

The 2-bit coding tag is designed to resonate at 75.5 GHz and 77.7 GHz with Q-factors of 298 and 287, respectively.

In order to create the final tag, this initial design is repeated 4 more times every 18° to surround the Luneburg lens. The layout of the model and the E-fields in and out of resonances
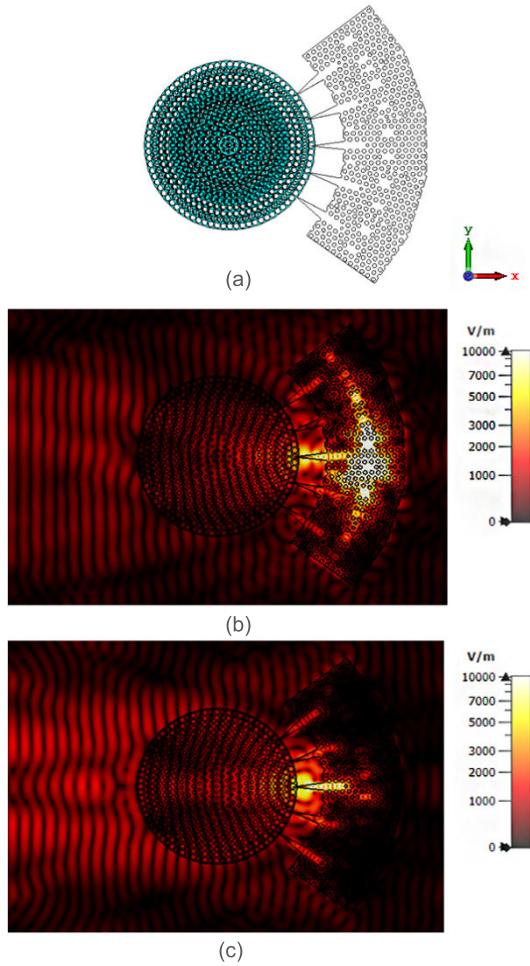
(a)

(b)

(c)

FIGURE 11. Model of Luneburg lens with five 2-bit resonator tags (a), electric field in resonance, f = 75.5 GHz (b), electric field out of resonance, f = 80 GHz (c).

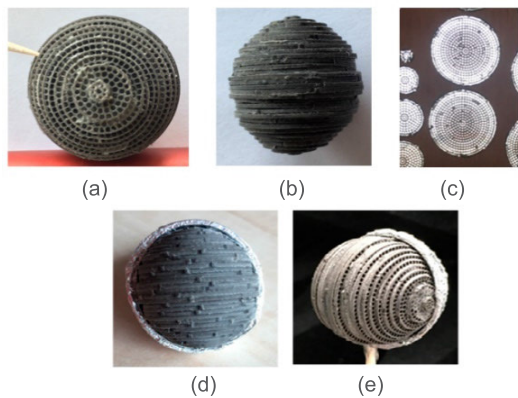(a)   (b)   (c)

(d)   (e)

FIGURE 12. Fabricated samples of Luneburg lens, top view (a), side view (b), perforated substrate layer (c), retroreflective lens - side view - azimuth (d), retroreflective lens - side view - elevation (e).

are shown in Fig. 11. A plane wave excitation with the wave propagation in the x direction and E vector in y direction to properly excite the PhC resonator tags is assumed.
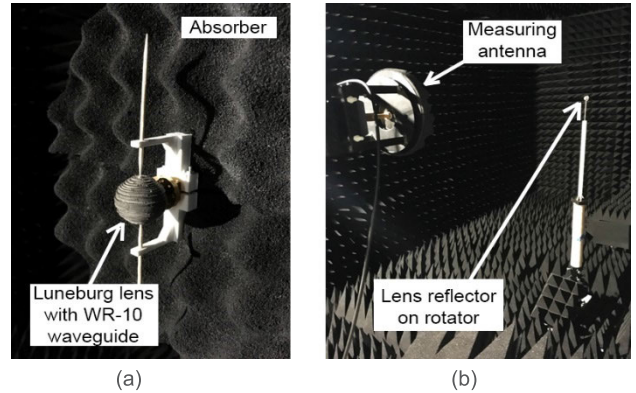

(a)   (b)

FIGURE 13. Measurement setup of Luneburg lens radiation pattern (a) and reflector's monostatic RCS (b).

IV. FABRICATION AND MEASUREMENTS

The Luneburg lens is fabricated by drilling the dielectric substrate Rogers RT5880. The holes are realized by the circuit board plotter LPKF ProtoMat S100. After removing copper, all 31 layers are manually cleaned and stacked together by a 30 μm thick double-sided tape. For the retroreflective Luneburg lens, a 3D printed plastic shell covered by a reflective aluminium foil is added to the back side of the lens as shown in Fig. 12.

A similar process is performed on the five 2-bit high-Q resonator tags. In this case, the dielectric substrate Rogers RT6010 (t = 1.27 mm, ε_r = 10.7, tan δ = 0.0023 [40]) is drilled and all copper is removed.

The measurement of the radiation pattern is performed in an anechoic chamber with the antenna scanner NSI 700S-30 and a Vector Network Analyzer (VNA) R&S ZVA67 with R&S ZVA-Z110E W-Band extensions. A standard WR-10 waveguide is used for the lens excitation and a 25 dBi WR-10 horn antenna is used as a receiving antenna (the measurement laboratory at Brno University of Technology). The lens is placed in front of the WR-10 waveguide with an air gap of 0.5 mm for proper focal area excitation. The arm with lens is then rotated in 1-degree steps by computer control.

The measurement of the monostatic RCS of the retroreflective Luneburg lens is performed with a WR-10 horn antenna, which serves as a transmitting and receiving antenna and the reflector is placed on a turntable at a distance of 1.3 m. The monostatic RCS is then calculated from the received power with and without the reflector. The flat plate reflector with a side length of 30 mm is used for calibration. The measurement setups are shown in Fig. 13 and the measured realized gain and monostatic RCS at a frequency of 80 GHz are shown in Figs. 14 and 15, respectively. The measurement was realized at a single frequency of 80 GHz with the dynamic range of RCS measurement setup of 60 dB.

The maximum measured gain of the Luneburg lens placed in front of a WR-10 hollow waveguide at 80 GHz is 24.31 dBi for azimuthal position (0 degree) and 24.62 dBi for elevation
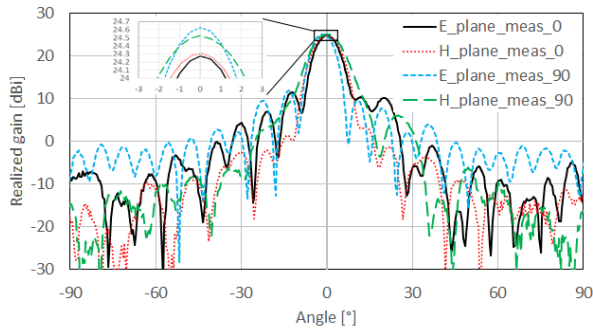
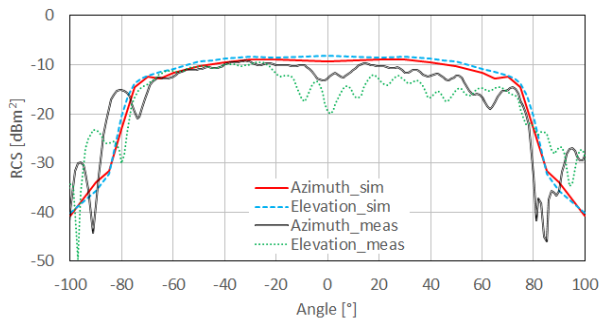**FIGURE 14.** Measured far-field radiation pattern of the perforated Luneburg lens.

FIGURE 15. Measured monostatic RCS pattern of the perforated Luneburg lens with reflective layer.

TABLE 2. Measured and simulated parameters of Luneburg lens antenna and retroreflector at a frequency of 80 GHz.

Luneburg lens			
Parameter	Measurement	Simulation	Lens Orientation
Realized gain E-plane	24.28 dBi	24.55 dBi	0°
	24.62 dBi	24.62 dBi	90°
Realized gain H-plane	24.31 dBi	24.55 dBi	0°
	24.53 dBi	24.62 dBi	90°
Side-lobe level E-plane	-13.4 dB	-14.8 dB	0°
	-13.5 dB	-15.3 dB	90°
Side-lobe level H-plane	-21.8 dB	-22.1 dB	0°
	-19.2 dB	-20.2 dB	90°
Retroreflective Luneburg lens			
RCS_{MAX}	-9.22 dBm^2	-8.93 dBm^2	Azimuth
	-9.47 dBm^2	-8.14 dBm^2	Elevation
Angular range (-6 dB)*	-69°–+72°	±75°	Azimuth
	±72°	±75°	Elevation

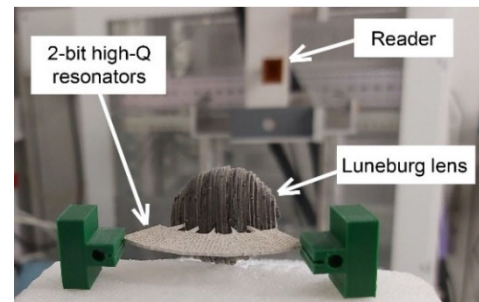*Not considering the local notches around 0° due to assembly inaccuracies of the reflective layer.

FIGURE 16. Monostatic RCS measurement setup of frequency-coded PhC retroreflective Luneburg lens with five 2-bit tags.

position (90 degree), respectively. Those values are in very good agreement with the simulations. The different value of realized gain can be caused by a shift of the focal area during the measurement due to lens rotation and by the slightly elliptical shape of the final lens. For the lens focal area shift of ±0.5 mm, the realized gain can vary about ±0.2 dB and the realized gain difference about −0.1 dB in azimuthal position can be expected. The measured side lobe levels in E-plane and H-plane are −13.4 dB and −21.8 dB in azimuthal position and −13.5 dB and −19.2 dB in elevation position, respectively. Ripples which are observed in the RCS patterns, are attributed to the combination of non-ideal alignment of the lens and reflector during the assembly (RCS drop about 2 dB), the irregular higher surface roughness in the range from 20 μm up to 450 μm, which can further reduce the RCS up to 0.8 dB and parasitic reflections inside the lens in combination with non-smooth profile of the reflective aluminium foil, which creates an additional parasitic air gaps (up to 1.5 mm) resulting in destructive wave interference and RCS drops (about 1 dB) at the given angles. Those combination of parasitic effects can reduce the RCS by at least 4 dB. The summary of measured results and comparison with simulation is presented in Tab. 2.

The measurement setup for the characterization of the tag landmark is shown in Fig. 16. A Vector Network Analyzer Agilent Technologies N5222A with an Anritsu 3740A W-Band extension and a 25 dBi WR-10 horn antenna is

used as a monostatic reader (the measurement laboratory at Technische Universität Darmstadt). The measurements are performed from 65 GHz to 110 GHz with 10001 frequency points and a dynamic range of 85 dB. The tag landmark consisting of the Luneburg lens and five 2-bit high-Q coding tags is placed on a turntable, and foam is used to adjust the height to that of the reader. The turntable and VNA are controlled by a computer, which rotates the tag landmark and measures the scattering parameter S_{11} at the antenna in 1-degree steps. For the characterization, a single measurement is performed without the lens and subtracted from the measured results to reduce the effect of the table on the measured response.

Additionally, an aluminum trihedral triangular corner retroreflector with 30 mm side length is used as a reference for the RCS calibration. The measured time-frequency response of the frequency-coded PhC Luneburg lens retroreflector is presented in Fig. 17. To obtain this figure, an inverse fast Fourier transform (IFFT) of the measured S-parameters at a certain incident angle is performed. Then, 200 signals are extracted by multiplying the time signal with 200 different rectangular windows of constant span while sweeping the
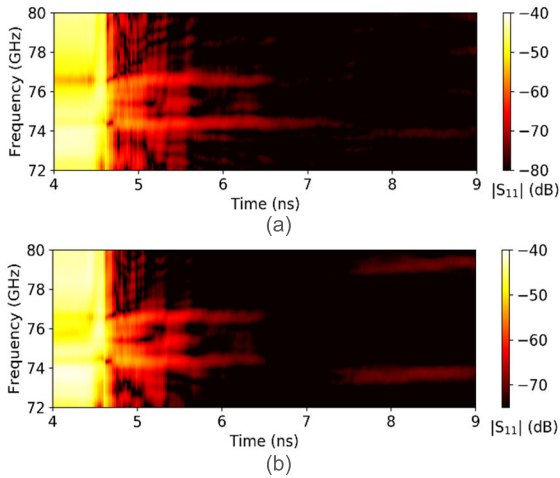
FIGURE 17. Time-frequency plot of the measurement realized with the frequency-coded PhC retroreflective Luneburg lens with five 2-bit tags at a distance of 70 cm for Luneburg lens orientation 0° (a) and 90° (b). The time-window span is 2 ns and the time values represent the start of the time window. The high-power wide-band reflection until t = 4.7 ns corresponds to the wideband structural reflection of the PhC tag.
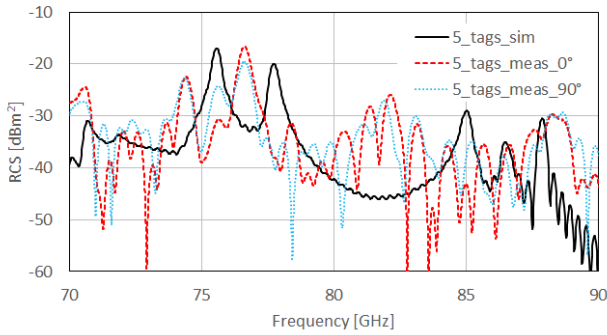

FIGURE 18. RCS frequency response of frequency-coded PhC retroreflective Luneburg lens with five 2-bit tags.

FIGURE 19. Measured monostatic RCS at 76.5 GHz of frequency-coded PhC retroreflective Luneburg lens with five 2-bit tags in (a) azimuth and (b) elevation for successive time windows starting at 4 ns (red), 4.9 ns (black), and 5.8 ns. The time-window span is 2 ns.

TABLE 3. Passive chipless frequency-coded mm-Wave retroreflectors.

RCS [dBm²]	Freq. [GHz]	Size [mm]	Q-factor	Measured distance [cm]	Ref.
-27.5	105.6	5.82 x 5.82 x 5.82	27	simulation	[3]
-5 to -30	90	30 x 30 x 30	< 50	100…400	[6]
-43.3	90.4	15.13 x 14.73 x 0.68	902	8.5	[16]
-15.8 to -40	76.5	25 x 25 x 25	240	70…130	This work

start times as indicated in the time-axis of the figure. Finally, each of these signals is transformed to the frequency domain with a Fast Fourier Transform (FFT). The FFT of each of the 200 extracted signals corresponds to one of the columns of data in Fig. 17.

The results of the tag landmark characterization are shown in Figs. 18 and 19. The resonance frequency of both resonators can be seen at 74.4 GHz and 76.5 GHz from the slower decay of the received power over time. Due to the long ringing, the signal from the resonators is received over a longer time, so that short clutter reflections can be differentiated from the response of the tag landmark. The observed frequency shifts between measured and simulated data can be caused by a slightly higher value of the relative permittivity of the used dielectric substrate.

Without the lens, the maximum readout distance between the reader antenna and the coding part is 15 cm. For larger distances, the received power is too low to be distinguished from background noise. With the lens, enough power is received to realize the characterization in the far-field of the horn antenna, so that measuring RCS can be performed. The
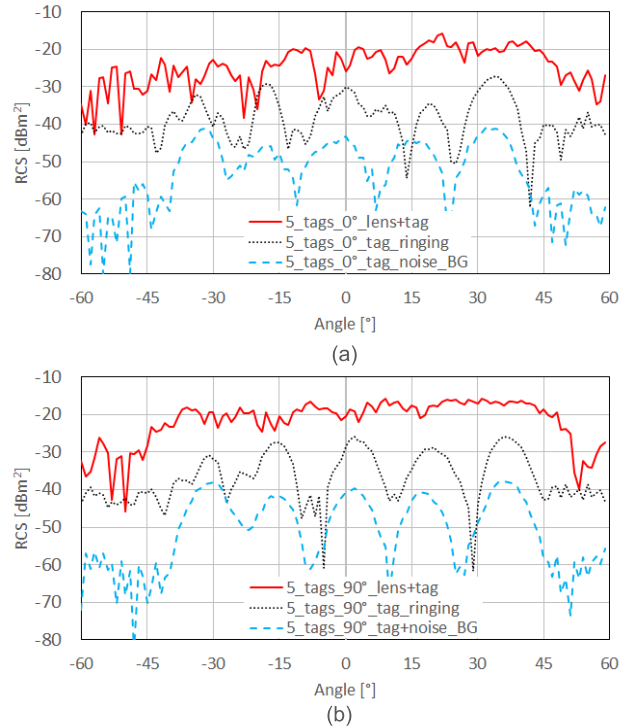
maximal measured RCS of the Luneburg lens with PhC as a reflective layer on the backside is −15.8 dBm², which is only about 7 dB lower in comparison to the aluminum foil backed Luneburg lens. Time gating is applied to see the resonance peaks, and RCS varies in a range from −15.8 dBm² to around −40 dBm² depending on the start of the time-gating window. A comparison to previous frequency-coded tags is summarized in Tab. 3. The maximum distance measured in laboratory is 130 cm as shown in Fig. 20.

The maximum range R_{max} of a monostatic radar system can be calculated by (7):

$$R_{max} = \sqrt[4]{\Delta P \frac{G^2 \lambda_0^2 \sigma}{(4\pi)^3}}, \qquad (7)$$

where $\Delta P = P_{transmit}/P_{receive}$ is the difference between the transmit power and the minimum receive power for
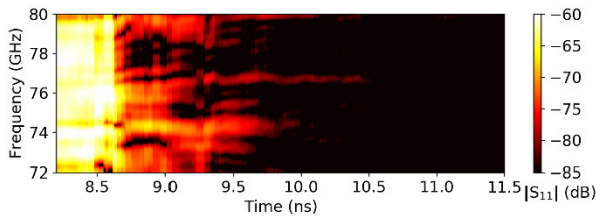
FIGURE 20. Time-frequency plot of the measurement realized with the frequency-coded PhC retroreflective Luneburg lens with five 2-bit tags at a distance of 130 cm. The time-window span is 2 ns and the time values represent the start of the time window. Compared to Fig. 18, the resonance frequencies of the high-Q resonators cannot be as clearly differentiated.
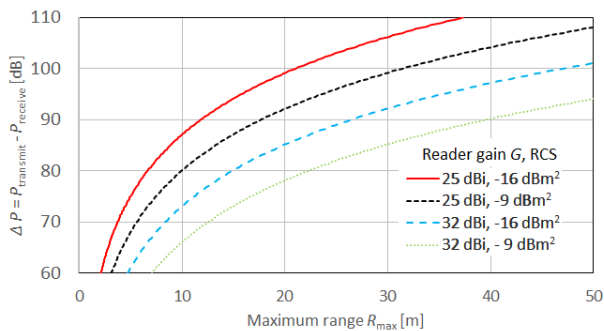

FIGURE 21. Link budget at 76.5 GHz for different RCS and reader gains. There is an equivalence between ΔP and $|S_{11}|$ in Fig. 18 and Fig. 21.

successful detection, G is the antenna gain of the monostatic reader, and σ is the RCS. A realistic calculation of maximum ranges is shown in Fig. 21.

Assuming $+10$ dBm transmitter output power, -100 dBm sensitivity of receiver [41], and 20 dB signal-to-noise ratio (SNR) for successful detection, the maximum range for $\Delta P = 10 + 100 - 20 = 90$ dB, the line of sight readout distance at 76.5 GHz varies from 11 m to 40 m.

The performance of the tag can be further increased by realizing the high-Q coding tags in lower loss materials like 3D-printed alumina and micromachined HR-Si as presented in [16], [42]. With these tags, both higher RCS and higher Q-factors can be achieved. Higher RCS increases the received power, while higher Q-factors result in a lower decay of the power over time, i.e., longer gating possible for the same SNR. In addition, the ripple observed in the RCS over the angle in Fig. 19 needs to be reduced and the number of bits of information, i.e. the number of high-Q resonators, increased. These current limitations can be addressed by optimizing the position of the resonators and reducing the distance between the dielectric rod antennas.

V. CONCLUSION

In this article, we presented a perforated Luneburg lens retroreflector for millimeter-wave frequency-coded indoor localization. The maximum realized gain of the lens without a reflective layer is 24.62 dBi and the reflector's monostatic RCS level is -9.22 dBm^2. In comparison with other commonly used retroreflectors, the retroreflective Luneburg lens

shows a very wide and stable RCS angular range of $\pm 72°$ over azimuth and elevation. By using this lens with five 2-bit high-Q resonator PhC frequency-coded tags at the backside, the maximum readout distance is increased from 0.15 m to 1.3 m at 76.5 GHz. Moreover, the lens with periodically arranged resonators around the lens as coding particles in a PhC structure demonstrates an angular range of $\pm 36°$, which can be increased by using more tags. Novel technologies such as alumina 3D printing will enable further increasing of the angular range in both planes, as well as reducing the losses in the coding part and increasing the Q-factor.

REFERENCES

[1] C. Händel, H. Konttaniemi, and M. Autioniemi, "State-of-the-art review on automotive radars and passive radar reflectors: Arctic challenge research project," Lapland Univ. Appl. Sci., Rovaniemi, Finland, Tech. Rep., 2018. [Online]. Available: https://www.lapinamk.fi/en/Cooperation/Publications?itemid=2403&showlocation=156780b2-7cff-495c-8179-9000c8cd11ec

[2] J. A. Vitaz, A. M. Buerkle, and K. Sarabandi, "Tracking of metallic objects using a retro-reflective array at 26 GHz," *IEEE Trans. Antennas Propag.*, vol. 58, no. 11, pp. 3539–3544, Nov. 2010.

[3] M. El-Absi, A. Alhaj Abbas, A. Abuelhaija, F. Zheng, K. Solbach, and T. Kaiser, "High-accuracy indoor localization based on chipless RFID systems at THz band," *IEEE Access*, vol. 6, pp. 54355–54368, 2018.

[4] T. Koonen, K. Mekonnen, F. Huijskens, N. Pham, Z. Cao, and E. Tangdiongga, "Recent advances in ultra-broadband optical wireless communication," in *Proc. Asia Commun. Photon. Conf. (ACP)*, Chengdu, China, Nov. 2019, pp. 1–3.

[5] J. Jebramcik, I. Rolfes, N. Pohl, and J. Barowski, "Millimeterwave radar systems for in-line thickness monitoring in pipe extrusion production lines," *IEEE Sensors Lett.*, vol. 4, no. 5, pp. 1–4, May 2020.

[6] A. Jimenez-Saez, M. Schusler, M. El-Absi, A. A. Abbas, K. Solbach, T. Kaiser, and R. Jakoby, "Frequency selective surface coded retro-flectors for chipless indoor localization tag landmarks," *IEEE Antennas Wireless Propag. Lett.*, vol. 19, no. 5, pp. 726–730, May 2020.

[7] K. Khourn, J. Liu, W. Noonpakdee, and S. Shimamoto, "Performance evaluation of optical wireless identification scheme employing thinfilm corner cube retroreflector," in *Proc. IEEE 24th Annu. Int. Symp. Pers., Indoor, Mobile Radio Commun. (PIMRC)*, London, U.K., Sep. 2013, pp. 3599–3604.

[8] J. Barowski, "Design and evaluation of a passive frequency-coded reflector using W-band FMCW radar," in *Proc. German Microw. Conf. (GeMiC)*, Cottbus, Germany, Mar. 2020, pp. 92–95.

[9] D. Eliyahu, L. S. Sadovnik, and V. A. Manasson, "Fratricide-preventing friend identification tag based on photonic band structure coding," *Proc. SPIE*, vol. 4029, pp. 337–346, Jul. 2000.

[10] K. Solbach, A. A. Abbas, M. El-Absi, A. Abuelhaija, and T. Kaiser, "Experimental demonstration of double-notch RCS spectral signature of corner reflector tag for THz self-localization system," in *Proc. 3rd Int. Workshop Mobile Terahertz Syst. (IWMTS)*, Essen, Germany, Jul. 2020, pp. 1–4.

[11] R. J. Williams, A. J. Gatesman, T. M. Goyette, and R. H. Giles, "Radar cross section measurements of frequency selective terahertz retroreflec-tors," *Proc. SPIE*, vol. 9102, May 2014, Art. no. 91020R.

[12] A. B. Numan, "Retroreflector and multibeam antenna for a millimeter wave collision avoidance system," Ph.D. dissertation, Dept. Elect. Eng., Polytechnique Montréal, Montréal, QC, Canada, 2018, Accessed: Sep. 20, 2020. [Online]. Available: https://publications.polymtl.ca/3035/1/2018_AhmedBilalNuman.pdf

[13] D. J. Thomson, D. Card, and G. E. Bridges, "RF cavity passive wireless sensors with time-domain gating-based interrogation for SHM of civil structures," *IEEE Sensors J.*, vol. 9, no. 11, pp. 1430–1438, Nov. 2009.

[14] B. Kubina, M. Schusler, C. Mandel, A. Mehmood, and R. Jakoby, "Wireless high-temperature sensing with a chipless tag based on a dielectric resonator antenna," in *Proc. IEEE SENSORS*, Baltimore, MD, USA, Nov. 2013, pp. 1–4.

[15] A. Jimenez-Saez, M. Schussler, M. Nickel, and R. Jakoby, "Hybrid time-frequency modulation scheme for chipless wireless identification and sensing," *IEEE Sensors J.*, vol. 18, no. 19, pp. 7850–7859, Oct. 2018.

[16] A. Jimenez-Saez, M. Schusler, D. Pandel, N. Benson, and R. Jakoby, "3D printed 90 GHz frequency-coded chipless wireless RFID tag," in *IEEE MTT-S Int. Microw. Symp. Dig.*, Bochum, Germany, Jul. 2019, pp. 4–6.

[17] A. Alhaj Abbas, M. El-Absi, A. Abuelhaija, K. Solbach, and T. Kaiser, "RCS enhancement of dielectric resonator tag using spherical lens," *Frequenz*, vol. 73, nos. 5–6, pp. 161–170, May 2019.

[18] A. Jiménez-Sáez, A. Alhaj-Abbas, M. Schüßler, A. Abuelhaija, M. El-Absi, M. Sakaki, L. Samfaß, N. Benson, M. Hoffmann, R. Jakoby, T. Kaiser, and K. Solbach, "Frequency-coded mm-wave tags for self-localization system using dielectric resonators," *J. Infr., Millim., Terahertz Waves*, vol. 41, no. 8, pp. 908–925, Jun. 2020.

[19] Y. Zhao, J. Weidenmueller, G. V. Bogel, A. Grabmaier, A. A. Abbas, K. Solbach, A. Jimenez-Saez, M. Schusler, and R. Jakoby, "2D metamaterial luneburg lens for enhancing the RCS of chipless dielectric resonator tags," in *Proc. 2nd Int. Workshop Mobile Terahertz Syst. (IWMTS)*, Bad Neuenahr, Germany, Jul. 2019, pp. 1–6.

[20] A. W. Doerry, "Reflectors for SAR performance testing," Sandia Nat. Laboratories, Albuquerque, NM, USA, Tech. Rep., 2008.

[21] C. S. Liang, D. A. Streater, J.-M. Jin, E. Dunn, and T. Rozendal, "A quantitative study of luneberg-lens reflectors," *IEEE Antennas Propag. Mag.*, vol. 47, no. 2, pp. 30–42, Apr. 2005.

[22] B. Dudley, "Design and manufacture of a low-profile radar retroreflector," in *Proc. Sensors Sensor Denial Camouflage, Concealment Deception RTO SCI Symp.*, Brussels, Belgium, 2004, pp. 1–39. Accessed: Aug. 21, 2020. [Online]. Available: https://apps.dtic.mil/dtic/tr/fulltext/u2/a456839.pdf

[23] L. A. Andrade, E. L. Nohara, G. G. Peixoto, M. C. Rezende, and I. M. Martin, "Backscattering analysis of flat plate and dihedral corner reflectors using PO and comparison with RCS measurements in anechoic chamber," in *IEEE MTT-S Int. Microw. Symp. Dig.*, Foz do Iguacu, Brazil, Sep. 2003, pp. 719–724.

[24] J. C. Deroba, K. D. Sobczak, A. Good, Z. Larimore, and M. Mirotznik, "Additively manufactured luneburg retroreflector," *IEEE Aerosp. Electron. Syst. Mag.*, vol. 34, no. 11, pp. 20–24, Nov. 2019.

[25] Y. G. Ma, C. K. Ong, T. Tyc, and U. Leonhardt, "An omnidirectional retroreflector based on the transmutation of dielectric singularities," *Nature Mater.*, vol. 8, no. 8, pp. 639–642, Aug. 2009.

[26] B. Yang and H. Friedsam, "Ray-tracing studies for a whole-viewing-angle retroreflector," in *Proc. 6th Int. Workshop Accel. Alignment (IWAA)*, Grenoble, France, 1999, pp. 1–12.

[27] A. Lundvall, F. Nikolajeff, and T. Lindström, "High performing micromachined retroreflector," *Opt. Express*, vol. 11, no. 20, pp. 2459–2473, 2003.

[28] J. Baker-Jarvis, E. J. Vanzura, and W. A. Kissick, "Improved technique for determining complex permittivity with the transmission/reflection method," *IEEE Trans. Microw. Theory Techn.*, vol. 38, no. 8, pp. 1096–1103, Aug. 1990.

[29] A. Aziz, L. Matekovits, and A. De Sabata, "A simple and robust technique to retrieve effective refractive index of heterogeneous dielectrics for millimeter-wave applications," in *Proc. Comput. Electromagn. Int. Workshop (CEM)*, Izmir, Turkey, Jul. 2015, pp. 1–2.

[30] H. F. Ma and T. J. Cui, "Three-dimensional broadband and broadangle transformation-optics lens," *Nature Commun.*, vol. 1, no. 1, p. 124, Dec. 2010.

[31] M. Liang, W.-R. Ng, K. Chang, K. Gbele, M. E. Gehm, and H. Xin, "A 3-D luneburg lens antenna fabricated by polymer jetting rapid prototyping," *IEEE Trans. Antennas Propag.*, vol. 62, no. 4, pp. 1799–1807, Apr. 2014.

[32] J.-M. Poyanco, F. Pizarro, and E. Rajo-Iglesias, "3D-printing for transformation optics in electromagnetic high-frequency lens applications," *Materials*, vol. 13, no. 12, p. 2700, Jun. 2020.

[33] Y. Xie, Y. Fu, Z. Jia, J. Li, C. Shen, Y. Xu, H. Chen, and S. A. Cummer, "Acoustic imaging with metamaterial luneburg lenses," *Sci. Rep.*, vol. 8, no. 1, p. 16188, Dec. 2018.

[34] A. Goulas, S. Zhang, J. R. McGhee, D. A. Cadman, W. G. Whittow, J. C. Vardaxoglou, and D. S. Engstrøm, "Fused filament fabrication of functionally graded polymer composites with variable relative permittivity for microwave devices," *Mater. Des.*, vol. 193, Aug. 2020, Art. no. 108871.

[35] Formlabs. *What Does Resolution Mean in 3D Printing?*. Accessed: Sep. 20, 2020. [Online]. Available: https://formlabs.com/blog/3d-printer-resolution-meaning/

[36] J. R. McGhee, T. Whittaker, J. Moriarty, J. Northedge, S. Zhang, D. Cadman, W. Whittow, and J. Y. Vardaxoglou, "Fabrication of artificial dielectrics via stereolithography based 3D-printing," in *Proc. 14th Eur. Conf. Antennas Propag. (EuCAP)*, Copenhagen, Denmark, Mar. 2020, pp. 1–5.

[37] N. Duangrit, B. Hong, A. D. Burnett, P. Akkaraekthalin, I. D. Robertson, and N. Somjit, "Terahertz dielectric property characterization of photopolymers for additive manufacturing," *IEEE Access*, vol. 7, pp. 12339–12347, 2019.

[38] A. C. Paolella, C. Corey, D. Foster, J. Desjardins, C. Smith, and L. Walters, "Broadband millimeter wave characterization of 3-D printed materials," in *IEEE MTT-S Int. Microw. Symp. Dig.*, Philadelphia, PA, USA, Jun. 2018, pp. 1565–1568.

[39] A. Jienez-Saez, M. Schubler, R. Jakoby, C. Krause, F. Meyer, and G. V. Bogel, "Photonic crystal THz High-Q resonator for chipless wireless identification," in *Proc. 1st Int. Workshop Mobile Terahertz Syst. (IWMTS)*, Duisburg, Germany, Jul. 2018, pp. 1–5.

[40] Rogers Corporation. *RT/Duroid 6006 and 6010 LM Laminate Data Sheet*. Accessed: Aug. 17, 2020. [Online]. Available: https://rogerscorp.com/-/media/project/rogerscorp/documents/advanced-connectivity-solutions/english/data-sheets/rt-duroid-6006-6010lm-laminate-data-sheet.pdf

[41] C. Mandel, "Approach for long-range frequency domain chipless RFID tags towards THz," in *Proc. Eur. Conf. Smart Objects, Syst. Technol.*, Duisburg, Germany, Jul. 2016, pp. 1–7.

[42] A. Jiménez-Sáez, "3D printed alumina for low-loss millimeter wave components," *IEEE Access*, vol. 7, pp. 40719–40724, 2019.

PETR KADERA (Graduate Student Member, IEEE) was born in Čeladná, Czech Republic, in 1994. He received the M.Sc. degree in electronics and communications from the Brno University of Technology, Czech Republic, in 2018, where he is currently pursuing the Ph.D. degree with the Department of Radio Electronics. His current research interests include 3D printing, artificial dielectrics, lens antennas, material characterization, and transformation optics in microwave and millimeter-wave frequencies.

ALEJANDRO JIMÉNEZ-SÁEZ (Graduate Student Member, IEEE) received the double master's degree (Hons.) in telecommunications engineering from the Polytechnic University of Valencia, Spain, and in electrical engineering from the Technische Universität Darmstadt, Germany, in 2017. He is currently pursuing the Ph.D. degree with the Institute of Microwave Engineering and Photonics, TU Darmstadt. His current research interests include chipless RFID, high-Q resonators, and electromagnetic bandgap structures in microwave and mm-wave frequencies.

TOM BURMEISTER received the B.Sc. degree in electrical engineering from the Technische Universität Darmstadt, Germany, in 2020, where he is currently pursuing the M.Sc. degree. He works as a Research Assistant with the Institute of Microwave Engineering and Photonics. His current research interests include high-Q resonators and chipless RFID.

MARTIN SCHÜßLER (Member, IEEE) received the Dipl.Ing. and Ph.D. degrees from the Technische Universität Darmstadt, Germany, in 1992 and 1998, respectively. He has been a Staff Member with the Institute for Microwave engineering and Photonics, Technische Universität Darmstadt, since 1998. During his career, he worked in the fields of III–V semiconductor technology, microwave sensors for industrial applications, RFID, and small antennas. His current research interests include microwave biosensors and passive chipless RFID.

ROLF JAKOBY (Member, IEEE) was born in Kinheim, Germany, in 1958. He received the Dipl.Ing. and Dr.Ing. degrees in electrical engineering from the University of Siegen, Germany, in 1985 and 1990, respectively. In 1991, he joined the Research Center of Deutsche Telekom, Darmstadt, Germany. Since 1997, he has been a Full Professor with the Technische Universität Darmstadt. He is the Co-Founder of ALCAN Systems GmbH. He is the author of more than 320 publications and holds 20 patents. His current research interests include tunable passive microwave devices, beam-steering antennas, chipless RFID sensor tags, and biomedical applicators, using metamaterial, ferroelectric, and liquid crystal technologies. He is a member of VDE/ITG and IEEE/MTT/AP societies. He received the Award from CCI Siegen for his excellent Ph.D., in 1992, and the ITG-Prize, in 1997, for an excellent publication in the IEEE Transactions on Antennas and Propagation. His group received 23 awards and prizes for best papers and doctoral dissertations. He was the Chairman of the EuMC in 2007 and GeMiC in 2011 and a Treasurer of the EuMW in 2013 and 2017. He is also the Editor-in-Chief of *Frequenz* (DeGruyter).

JAROSLAV LACIK (Member, IEEE) received the M.Sc. and Ph.D. degrees from the Brno University of Technology, Brno, Czech Republic, in 2002 and 2007, respectively. He is currently an Associate Professor with the Brno University of Technology. His research interests include antennas, body-centric wireless communication, computational electromagnetics, and measurement.

• • •